



NuSTAR

Instrument Performance Guide

Release 1.0

November 16, 2009

Document custodians: Fiona Harrison, Kristin Madsen

1. Introduction

This document is intended as a guide for the NuSTAR science team to use in preparing feasibility and observing time estimates. It provides a functional overview of the telescope, a description of the data products, and useful plots for making estimates of source counts, detection thresholds, etc.. ASCII text files with background rates and effective area are available. For detailed simulations involving spectral fitting, we recommend using the ARF and RMF files in conjunction with XSPEC.

The performance specifications in this document are based on current best estimates made by the instrument team. It should be noted that these projections may change as ground calibration and test data become available for engineering test articles and flight hardware. We expect that these will reflect the on-orbit performance to 20% in the case of effective area, 5% in case of detector efficiencies, and 30% in the case of internal background. The uncertainties are due to our lack of knowledge of some model parameters. For example the on-orbit particle environments, obscuration factors for the optics, number of dead pixels in the focal plane, and correlations between thermal distortions in the telescope structure are difficult to know with a high degree of accuracy prior to calibration of the flight hardware and/or on-orbit measurements. Feasibility estimates should be performed with these uncertainties in mind.

2. Functional Overview

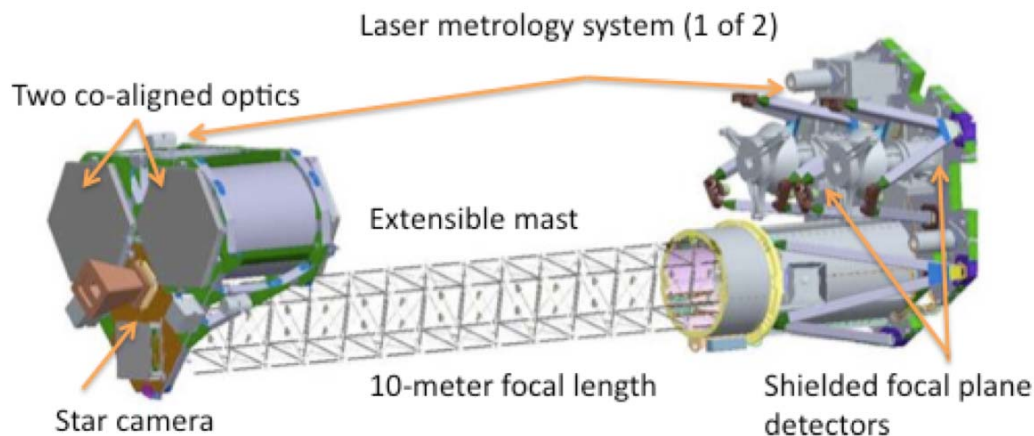


Figure 1: Principal instrument components

The NuSTAR instrument consists of two co-aligned focusing hard X-ray telescopes. The telescopes have a 10-m focal length, fixed by an extendible mast that deploys after launch. The instrument has built in aspect and alignment metrology, provided by a laser alignment system and a star tracker head mounted on the optics bench. Table 1 provides a summary of the principal instrument performance characteristics.

Parameter	Value	Parameter	Value
Energy band	5 – 80 keV	Strong src. localization	1.5" (1- σ)
Half Power Diameter	43"	Temporal resolution	0.1 msec
PSF FWHM	7.5"	ToO latency	2 – 24 hr
Energy resolution (FWHM)	0.6 keV@10 keV 1.2 keV @ 68 keV	Field of View (50% area)	10' @ 10 keV 8' @ 40 keV 6' @ 68 keV

Table 1: Key Parameters

Detailed design documents for all elements of the instrument are being developed and will be available to the team as they are finalized. In this report we provide a basic functional description, an overview of the principal parameters, and point out some the differences between NuSTAR and soft X-ray telescopes such as ASCA, XMM and Chandra.

2.1 Optics

The optics consist of highly-nested, low graze angle, multilayer coated shells in a conical approximation of a Wolter-I geometry. Compared to soft X-ray telescopes, the NuSTAR optics have a smaller average graze angle (angle between the incident X-ray and the optics shell), and therefore a smaller field of view. Due to the tightly nested, small graze angle design, the vignetting is noticeable over the sensitive field (as defined by the focal plane detector area), so that the effective area falls towards the edge of the FoV. Because the reflectance is dependent on the graze angle and energy (higher energies are more effectively reflected at smaller graze angle), the FWHM of the optics area as a function of off-axis angle decreases with X-ray energy.

Parameter	Value	Parameter	Value
Focal length	10.14 m	Shell length	22.5 cm
# shells	130	Min. graze angle	1.34 mrad
# azimuthal segments	6 (inner)/12 (outer)	Max. graze angle	4.7 mrad
Inner radius	5.44 cm	Coating (outer)	W/Si
Outer radius	19.1 cm	Coating (inner)	Pt/SiC

Table 2: Principal optics design parameters

The optics are coated with depth graded multilayer structures which, for energies above ~15 keV, increase the graze angle for which significant reflectance can be achieved. This increases the field of view and high –energy collecting area relative

to standard metal coatings. The coating materials and prescriptions vary as a function of graze angle (or equivalently shell radius). Variations in the telescope effective area can be seen at the Tungsten and Platinum K-absorption edges at 69.5 and 78.4 keV.

The NuSTAR optics have angular response dominated by figure errors inherent in the substrates and in the mounting technique. As a result, unlike Chandra, the point spread function is not a strong function of off-axis angle. The detailed shape will change, but to first order the area of the encircled energy contours will remain approximately constant.

2.2 Focal Plane

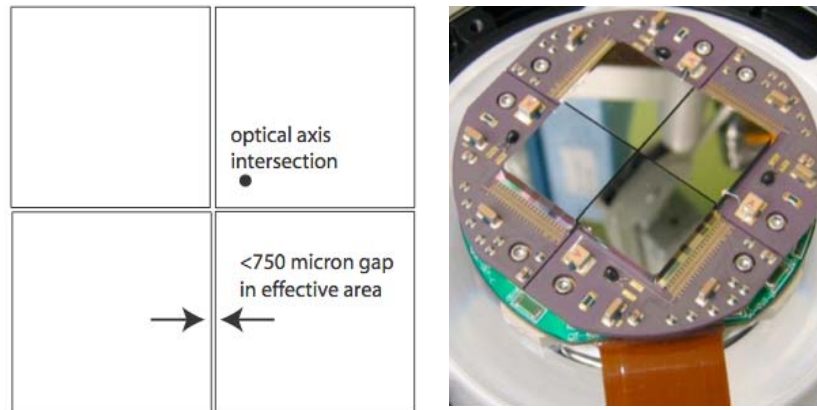


Figure 3: NuSTAR focal plane layout

The focal plane of each NuSTAR telescope consists of a 2 x 2 array of imaging CdZnTe pixel detectors. The hybrid detectors consist of a 2-mm thick $\text{Cd}_{0.9}\text{Zn}_{0.1}\text{Te}_{1.0}$ crystal connected to a custom integrated circuit. The optical axis intersects the detectors off-center, so as to avoid the dead area between detectors. Each of the four detectors has a 32 x 32 array of pixels on a 0.6 mm pitch. This corresponds to an subtended angle on the sky of 12.3"/pixel. The dead gap between detectors is nominally 0.5 mm, but will not exceed 0.75 mm.

Parameter	Value	Parameter	Value
Pixel size	0.6mm/12.3"	Max processing rate	350 evt/s ⁻¹
Focal plane size	13' x 13' square	Max flux meas. rate	10 ⁴ cts/s
Detector format	32 x 32	Time resolution	2 microsec
Energy threshold	3 keV (each pixel)	Dead time frac (@thresh)	<5%

Table 3: Focal Plane parameters

The pixel detectors have readout electronics that trigger each time an X-ray is detected. The event is immediately read out and processed. After processing on the ground, each event is tagged with an energy, time (digitized to 2 microseconds), and interaction pixel. The NuSTAR detectors do not employ an integrating CCD-style readout, so that pulse pileup will not occur until source fluxes of $\sim 10^5$ cts/s/pixel. The processing time per event is 2.5 milliseconds, limiting the rate at which events can be read out to between 300 and 400 evts/s. Each event has the live time since the previous event recorded to an accuracy of 1 microsecond, so that fluxes can be measured to 1% accuracy even for incident count rates of 10^4 cts/s.

3. Effective Area and Field of View

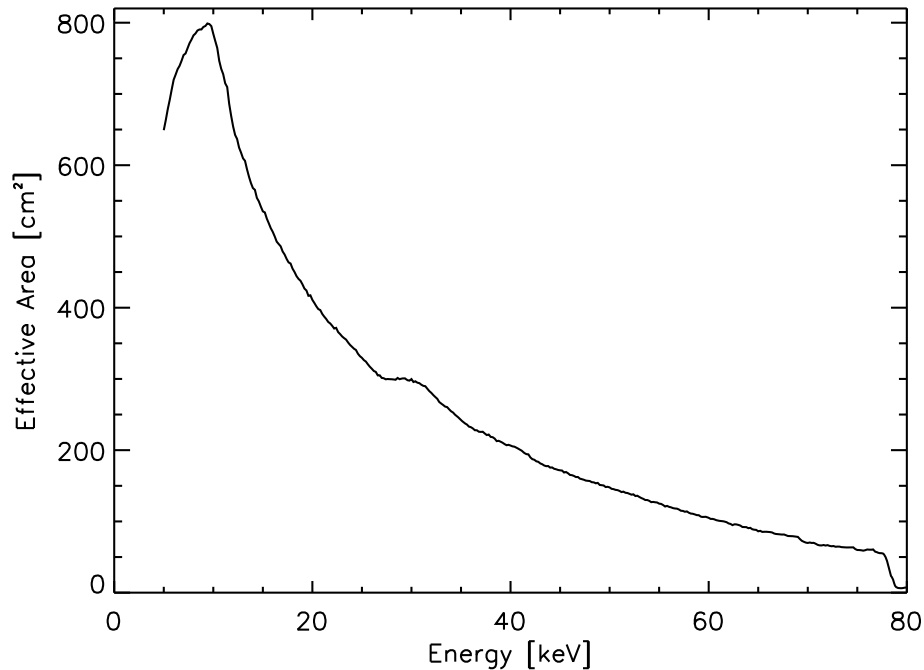


Figure 4. Telescope on-axis effective area as a function of energy. This figure includes two telescopes, thermal blanketing, detector entrance window, and detector quantum efficiency.

As discussed above, the telescope collecting area is a function of energy and off-axis angle. The low energy threshold is determined by the detector pixel trigger threshold of ~ 3 keV. Between 3 and 6 keV the detector quantum efficiency steadily increases because events with energy split among pixels become more easily detected. In addition, the telescope collecting area increases with energy between 5 – 10 keV as the optics thermal covers and detector entrance windows become more transparent. Above 10 keV the area decreases with energy due to decrease in reflectance of the coatings above the critical angle for total external reflection.

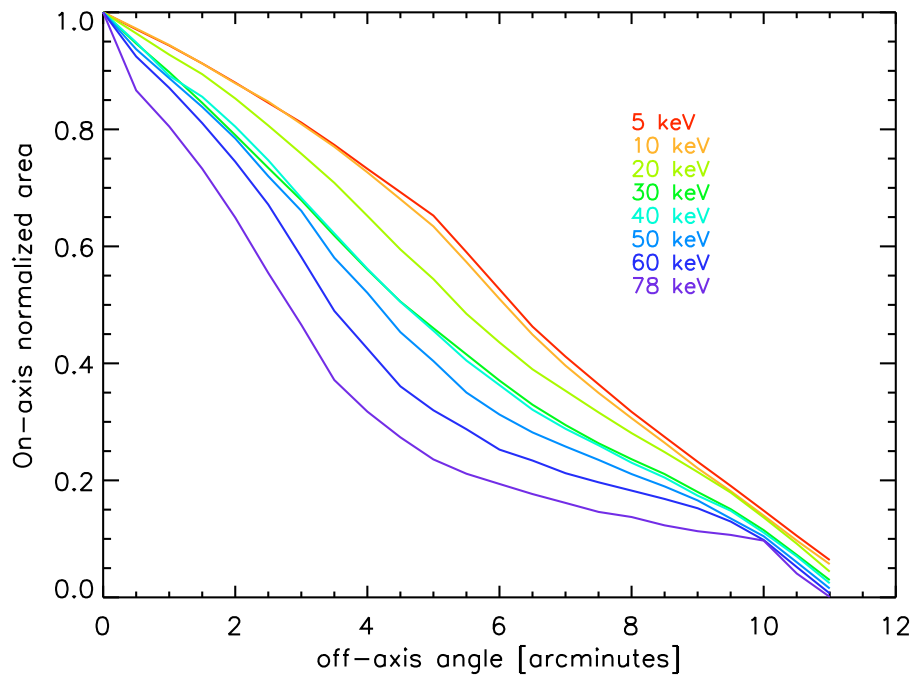


Figure 5. Collecting area as a function of off-axis angle for several energies. The edge of the detector is at $6.5'$ off axis, and the corners are $9'$ off-axis.

4. Point Spread Function

The point spread function (PSF) of the optics is sharply peaked and has broad wings. The PSF is modeled using a King's profile as a convenient parameterization. If detector sampling is ignored, the FWHM of the PSF is $7.5''$, while the half power diameter (HPD), defined as the diameter of the circle enclosing 50% of the flux, is currently estimated to be between 40 and $45''$. Figure 6 shows the profile of the PSF, and Figure 7 plots the integrated function. Table 4 provides a few points on the integrated curve.

Because of the shape of the PSF, the optimal extraction radius for source detection is smaller than for Chandra. In the background limited case (integrations longer than $\sim 10^5$ s) an extraction radius of 50% is optimal.

Encircled energy fraction	Diameter (arcsec)
50%	43
70%	75
80%	101

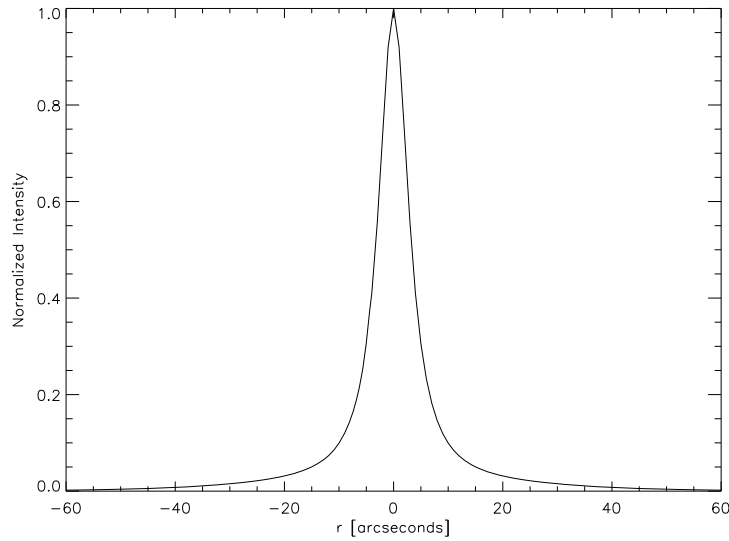


Figure 6: Point spread function. The PSF has a sharp core and broad wings. 50% of the flux from a point source is enclosed in a diameter of 45", while the FWHM is 7.5".

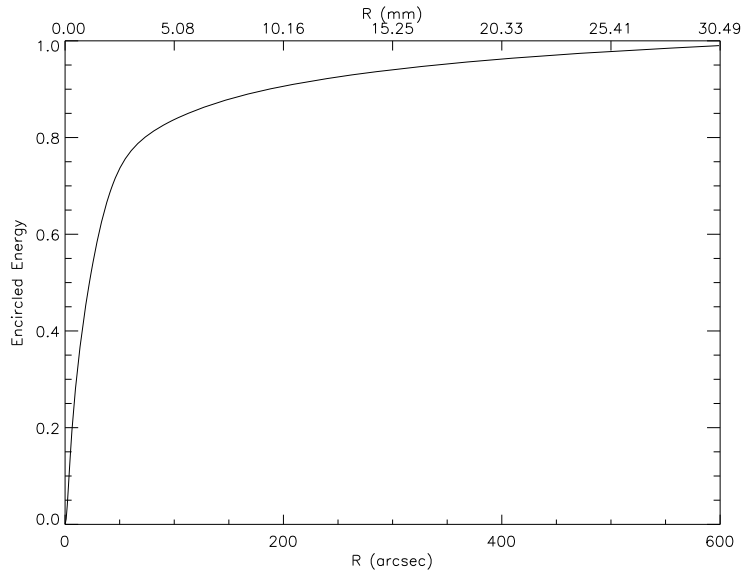


Figure 7. Integrated PSF. The half power diameter (diameter at which half the flux is enclosed) is 45 arcseconds.

5. Detector Response Matrix

X-rays interact in the detector predominantly through photoelectric absorption, which leads to ejection of a L- or K-shell electron from Cd or Te. The electron excites charge carriers (electron-hole pairs) in the crystal which drift to the electrodes as the result of a constant bias maintained between the pixel anodes and the top cathode. The magnitude of the signal depends on the energy of the original X-ray. Because charge diffuses as it traverses the 2mm thick detector, events that interact near pixel edges will trigger multiple pixels. Events are assigned a grade based on how many pixels are triggered. Spectra made using single pixel events will have the best energy resolution at the expense of quantum efficiency.

If the incident X-ray is above the K-shell binding energy for Cd or Te (26.7 and 31.8 keV respectively), a fluorescent X-ray with significant energy (23.2 for Cd and 27.5 keV for Te) will be emitted coincident with the absorption. This can lead to off-diagonal terms in the response matrix that result from escape of the fluorescent X-rays from the detector volume. Thus, the “photopeak” efficiency – ie the efficiency of absorption with full energy deposition in the detector – differs from the quantum efficiency – or fraction of events registering a trigger in the detector.

The detection quantum efficiency is high over the entire energy band, while the photopeak efficiency (defined by the response matrix integrated within 2-sigma of the peak) varies with energy, decreasing above the K absorption edges. Table 4 shows the detection and photopeak efficiencies at various energies.

Energy (keV)	Detection efficiency	Photopeak efficiency
10	0.96	0.95
30	0.95	0.90
40	0.96	0.86
60	0.97	0.89
70	0.96	0.89

Table 4: Detector efficiency

The spectral resolution varies with energy due to charge trapping effects in the detector. At low energy ($E \lesssim 20$ keV) the resolution is dominated by electronic readout noise, and is 600 – 800 eV FWHM. At higher energy the resolution is dominated by charge trapping, and is 1.0 – 1.2 keV FWHM at 60 keV.

6. Background

Background consists of diffuse cosmic flux that enters through the aperture stop and internal detector background. The aperture component is significantly larger than the focused diffuse cosmic flux that enters through the optics. The internal background has been determined through Monte Carlo simulations using GEANT 3 and MGGPOD. The background count rates in relevant extraction radii determined for the 5° inclination LEO are provided in Table 5

Table 5: Background count rate in extraction regions of various sizes.

Bkg (cts/s)	in HPD (2 telescope)	70% enc en diam	80% enc en diam
6 – 10 keV	3.4×10^{-4}	9.8×10^{-4}	$17. \times 10^{-4}$
10 – 30 keV	6.8×10^{-4}	18×10^{-4}	32×10^{-4}
30 – 60 keV	4.0×10^{-4}	11×10^{-4}	18×10^{-4}
67 – 70 keV	0.34×10^{-4}	0.94×10^{-4}	1.7×10^{-4}

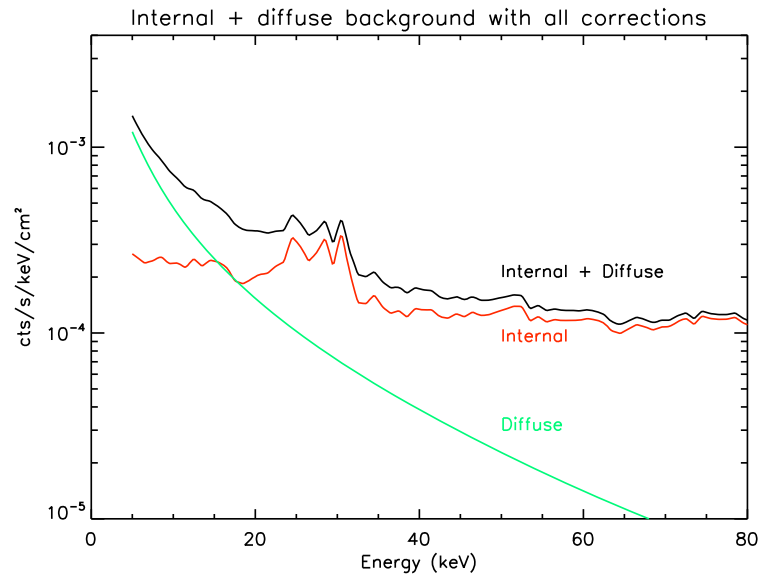


Figure 8: Background count rate per unit area on the detector as a function of energy.

7. Sensitivity

The figure below shows sensitivity limits as a function of time for on-axis sources for three energy bands. Limits are shown for detection and flux measurement at the 4-sigma confidence level. Detection limits are appropriate if the objective is to identify previously unknown sources for followup. The detection limit uses the Poisson probability distribution to determine if a concentration of counts is significant above background. For short integrations where background is negligible this will differ significantly from a Gaussian probability. We always require 5 photons for a detection, even when the background approaches zero. Flux detection limits use a Gaussian probability distribution (ie \sqrt{N}). The equivalent of a 3.7-sigma confidence level ensures <1% false identification rate – we adopt 4-sigma for all plots.

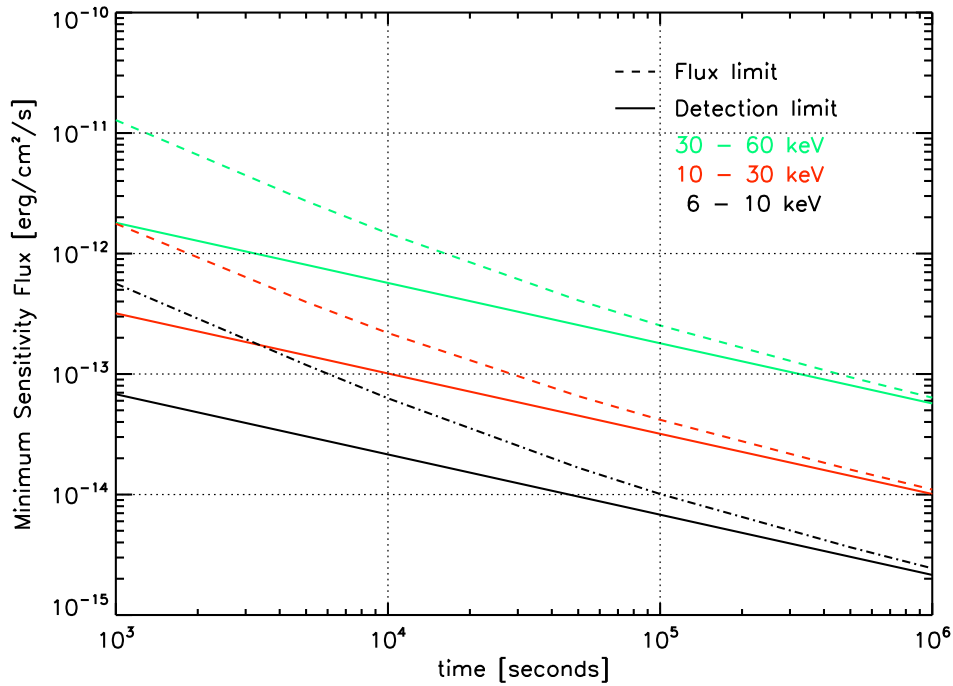


Figure 9. On-axis detection (4-sigma) and flux measurement sensitivity for several energy bands as a function of integration time.

8. Sky Mapping Sensitivity

Because the effective area decrease off axis is a function of energy, the uniformity with which a large (many times the FoV) survey area is mapped will typically depend on energy. Various strategies can be adopted ranging from having non-overlapping fields, and therefore non-uniform depth, to highly overlapping fields of view. Figure 10 shows the uniformity of depth achieved for the 6 – 10 keV band for mapping a $\sim 1 \text{ deg}^2$ area in two months of observation time using three different strategies. The first assumes tiling with non-overlapping fields of view, the second assumes a corner shifting, and the third shifting by half the field of view. An observing efficiency of 60% is assumed. Plots of depth vs. sky coverage for 0.5, 1, 2, 4, and 6-month observation times (including efficiency) are also shown for 6-10, 10-30 and 30-60 keV bandpasses in Figures 11-15. The plots assume a 4-sigma detection threshold, which would ensure <1% rate of spurious source detections for blind source searches.

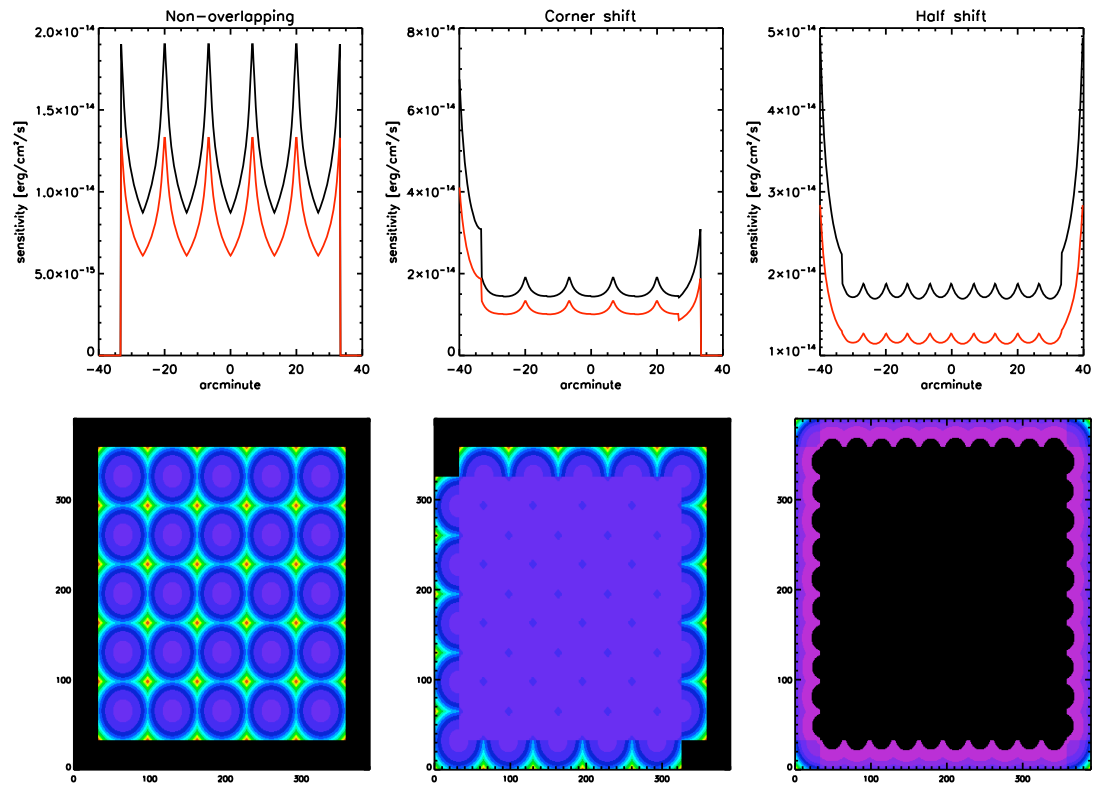


Figure 10: Depth for mapping an area of $\sim 1 \text{ deg}^2$ in one month (clock time) in the 6-10 keV band for several different tiling strategies.

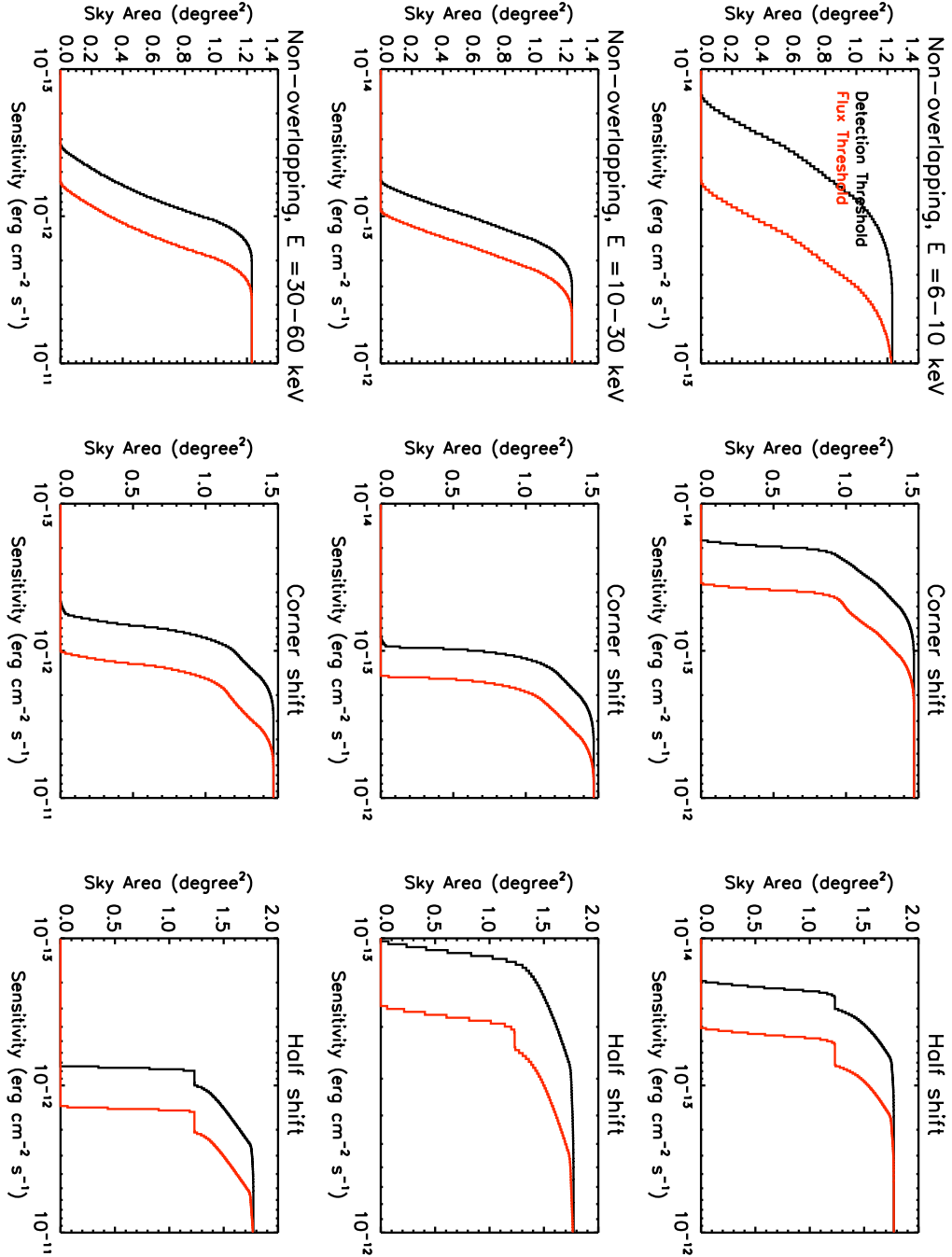


Figure 11: Depth in three bands (6- 10, 10 - 30, 30 - 60 keV) for three mapping strategies covering ~ 1 deg² in 0.5 months (clock time). The black line shows detection sensitivity (4-sigma, <1% misidentification rate), and the red line shows flux measurement sensitivity (4-sigma).

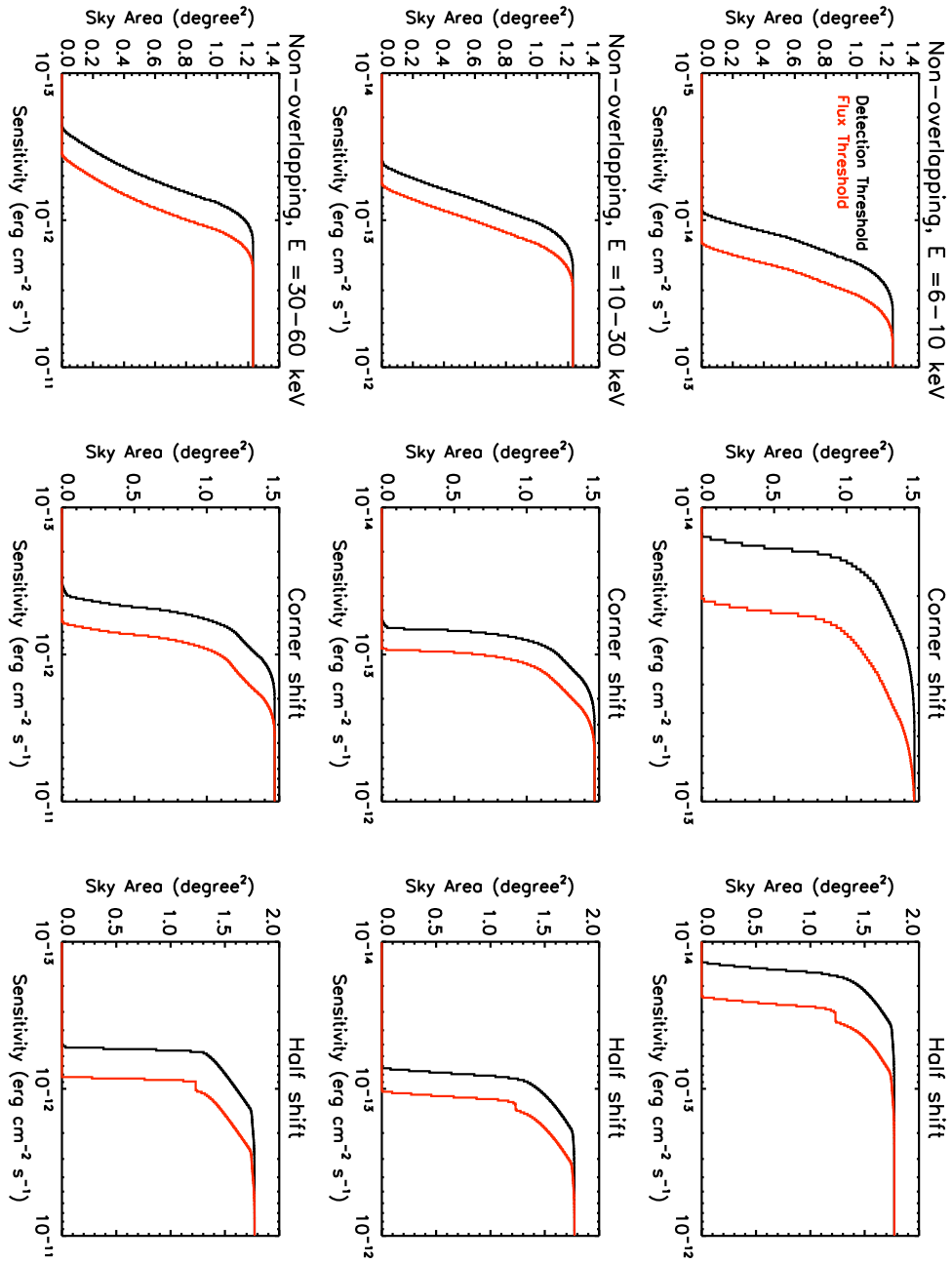


Figure 12: Depth in three bands (6- 10, 10 - 30, 30 - 60 keV) for three mapping strategies covering $\sim 1 \text{ deg}^2$ in 1 months (clock time). The black line shows detection sensitivity (4-sigma, $< 1\%$ misidentification rate), and the red line shows flux measurement sensitivity (4-sigma).

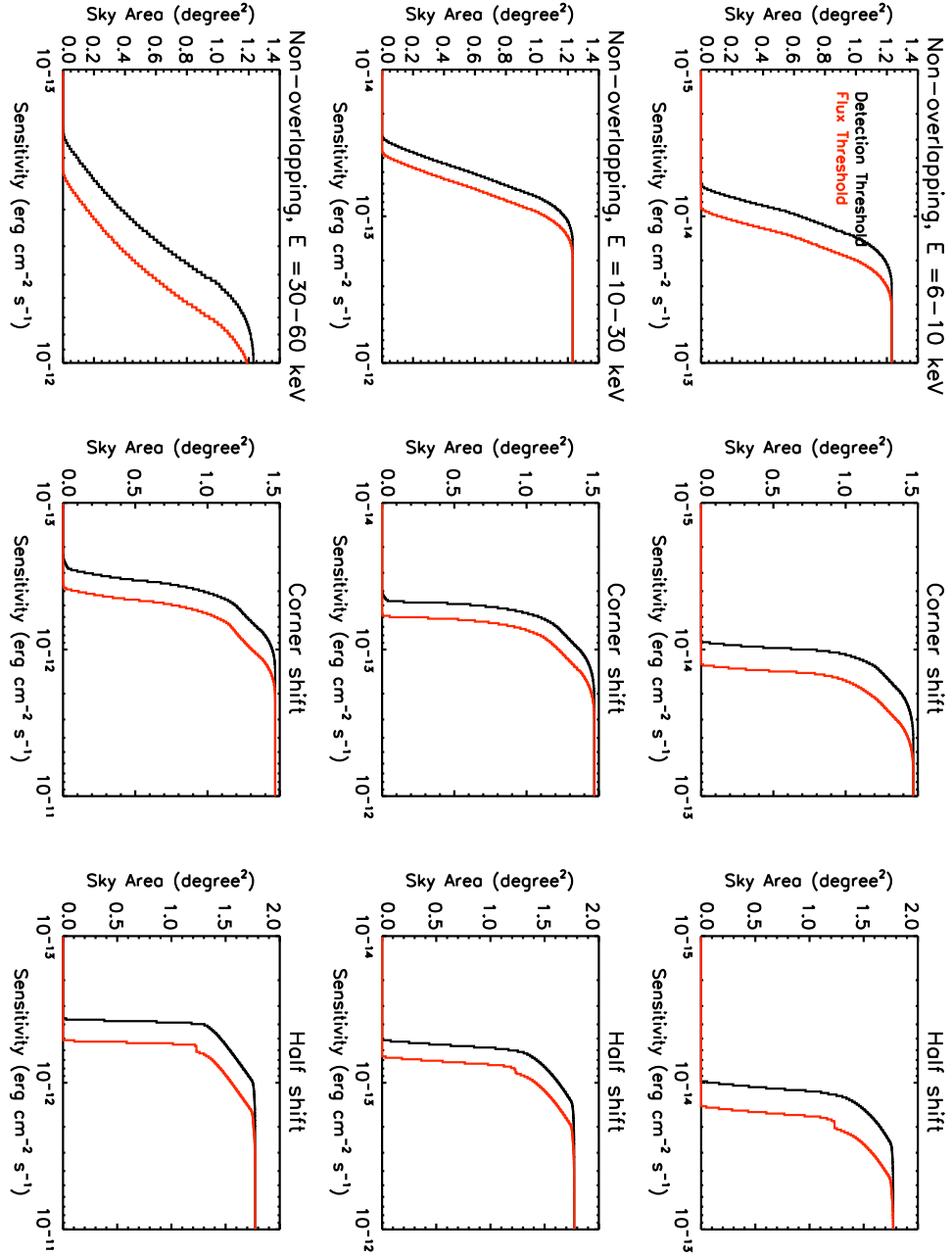


Figure 13: Depth in three bands (6- 10, 10 - 30, 30 - 60 keV) for three mapping strategies covering ~ 1 deg² in 2 months (clock time). The black line shows detection sensitivity (4-sigma, <1% misidentification rate), and the red line shows flux measurement sensitivity (4-sigma).

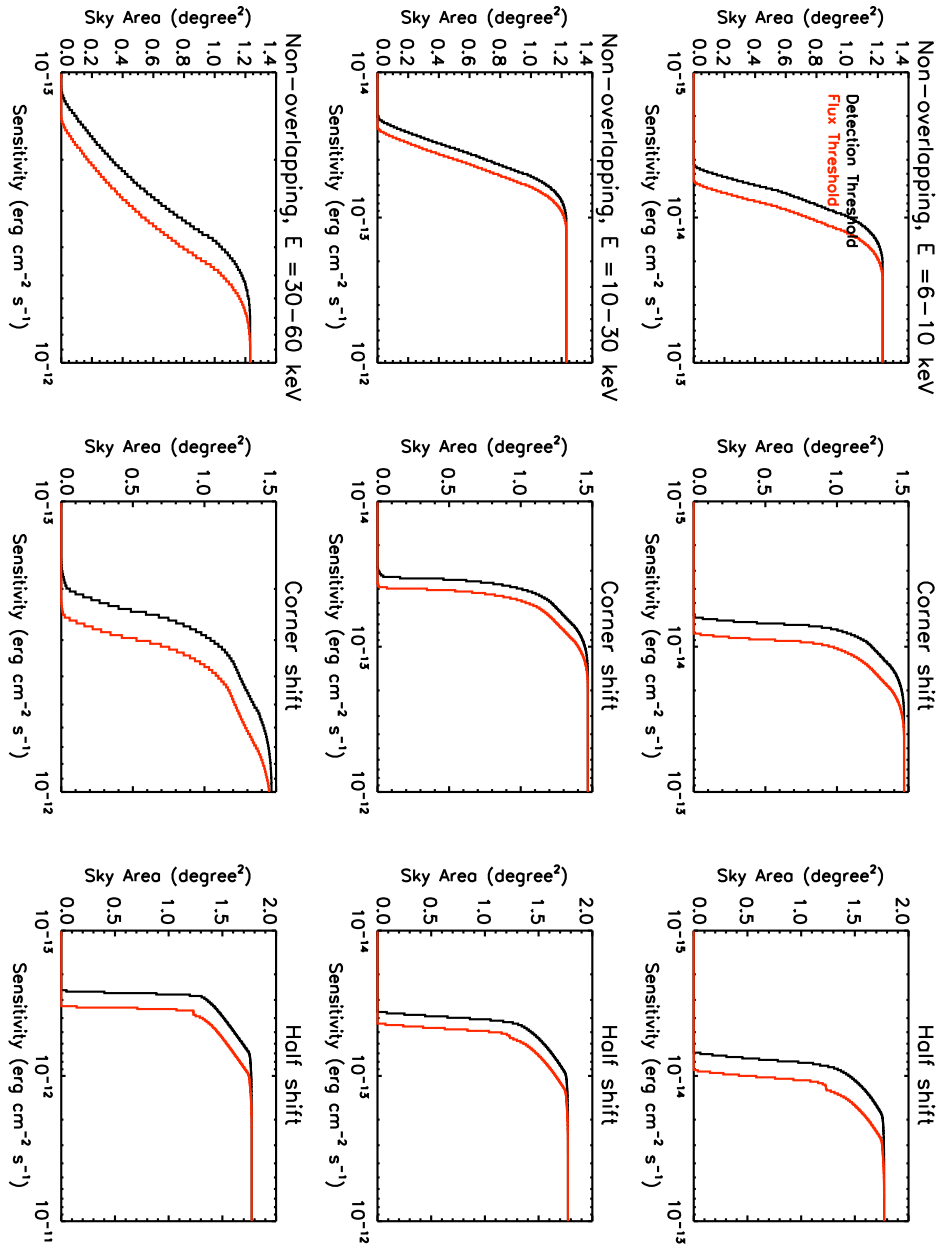


Figure 14: Depth in three bands (6- 10, 10 - 30, 30 - 60 keV) for three mapping strategies covering $\sim 1 \text{ deg}^2$ in 4 months (clock time). The black line shows detection sensitivity (4-sigma, <1% misidentification rate), and the red line shows flux measurement sensitivity (4-sigma).

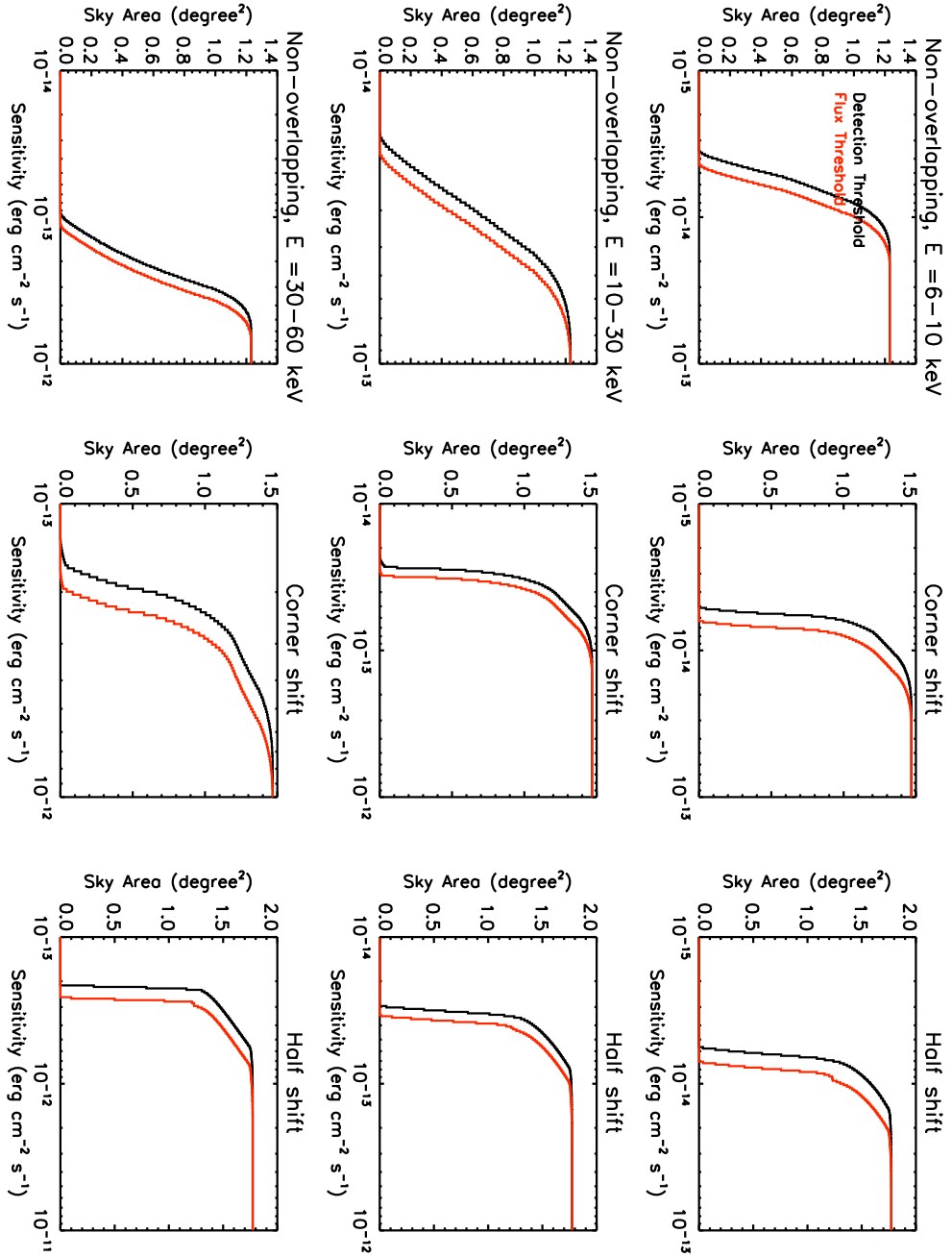


Figure 15: Depth in three bands (6- 10, 10 - 30, 30 - 60 keV) for three mapping strategies covering ~ 1 deg² in 6 months (clock time). The black line shows detection sensitivity (4-sigma, <1% misidentification rate), and the red line shows flux measurement sensitivity (4-sigma).

8. Source Positioning

The systematic contribution to source positioning is 3" at 90% confidence. For faint sources, statistical variations dominate. Simulations are underway to determine source positioning accuracy as a function of signal to noise of detection.

9. Confusion Limits

[This section under construction].

The HPD is 43", the FWHM is 7.3". Different limits will apply for confusion limits where flux measurement is compromised vs. source positioning. Simulations need to be undertaken to quantify these limits.

10. Observing Efficiency

Observing efficiency includes contributions from slew and settling times, Earth occultations, SAA passage, and detector dead time. The minimum observation times will be ~2 weeks, and the slew and settling times are short – the nominal slew rate is 1.2°/minute with settling times of a few minutes – so that Earth occultations, SAA passage and dead time are the dominant contributions. The effect of occultations depends on angle of the source from the celestial pole. For most fields without bright sources (ie nominal dead time), the total observing efficiency will be between 57 and 60%, although for a few fields (e.g. GOODS-N) the efficiency will be 75%, and for a small number of targets (1987A, M82) it exceeds 90%. For fields with bright sources, the dead time will become a significant contribution. Table 6 shows the dead time fraction as a function of count rate.

R (1 telescope) cps	DTF (CBE)(%)
7	3.7
10	4.3
50	12
100	21.4
200	40.5
400	78.6

Table 6: Instrument dead time as a function of count rate in a single telescope.